SCIENTIFIC REPORTS

OPEN

SUBJECT AREAS:
SENSORS
ELECTRONIC DEVICES

Received
30 January 2014

Accepted
20 March 2014

Published
10 April 2014

Correspondence and requests for materials should be addressed to Q.L. (liqiuhong2004@hotmail.com) or T.W. (thwang@xmu.edu.cn)

Surrounding Sensitive Electronic Properties of Bi_2Te_3 Nanoplates—Potential Sensing Applications of Topological Insulators

Bin Liu[1], Wuyuan Xie[2], Han Li[1], Yanrong Wang[1], Daoping Cai[1], Dandan Wang[1], Lingling Wang[1], Yuan Liu[1], Qiuhong Li[1] & Taihong Wang[1]

[1]Pen-Tung Sah Institute of Micro-Nano Science and Technology of Xiamen University, Xiamen361005, China, [2]Department of Physics, School of Physics and Mechanical & Electrical Engineering, Xiamen University, Xiamen361005, China.

Significant efforts have been paid to exploring the fundamental properties of topological insulators (TIs) in recent years. However, the investigation of TIs as functional materials for practical device applications is still quite limited. In this work, electronic sensors based on Bi_2Te_3 nanoplates were fabricated and the sensing performance was investigated. On exposure to different surrounding environments, significant changes in the conducting properties were observed by direct electrical measurements. These results suggest that nanostructured TIs hold great potential for sensing applications.

Topological insulators (TIs) are materials with gapped insulating bulks and metallic conducting surfaces[1,2]. The strong spin-orbit coupling in TIs reduces the probability of the electrons being backscattered by surface defects, which lowers the surface resistivity and leads to the formation of topologically protected surface states[3,4]. This special spin helical Dirac transport regime makes TIs promising for a number of novel applications such as spintronics and quantum computing[4,5,6]. The recently discovered three-dimensional (3D) TIs such as Bi_2Se_3 and Bi_2Te_3 which are referred to as the second generation of TIs open up new possibilities for device applications[2,7,8]. This is because these 3D TIs are composed by layered structures in which the adjacent layers are bonded together by weak van der Waals forces, thereby enabling mass production by both top-down mechanical exfoliation[9,10] and bottom-up chemical synthesis[11,12,13,14]. But nowadays the substantial bulk carrier density is still a major challenge, hence enhancing the surface conduction is critical. Making TIs into nanostructures is a simple but effective strategy because the large surface to volume ratios of nano-scaled materials can maximize the surface contribution to the total conduction[15,16]. So nanostructured TIs may have wider potential applications than bulk single crystals due to the reduced bulk conduction[15,17,18].

Device applications do require detailed investigation on the electric and dielectric properties of the material under different conditions, as the practical operating environment can be quite diversified. The chemical doping effect of gas molecules on TIs has drawn much attention because of its potential applications in tuning the transport properties of TI based devices. It has been demonstrated that the energy position of the Dirac point (E_D) in TIs can be tuned by dosing with certain gas molecules[4,19,20]. Reducing gases such as H_2 and CO serve as n-type doping agents[20] while oxidizing ones such as O_2 and NO_2 serve as p-type doping agents[4]. All these experimental evidences are obtained using non-transport, surface sensitive techniques such as angle resolved photoemission spectroscopy (ARPES) and scanning tunneling microscopy (STM)[21]. However, these techniques are difficult to be used in portable applications because of the large size and high cost of the equipment. Therefore, investigating the material properties by direct electrical measurement is of fundamental importance for device development and innovation.

In this work, single-crystalline Bi_2Te_3 nanoplates (NPs) are synthesized through a solvothermal route. The crystal structure and growth orientation are analyzed by high resolution transmission electron microscopy (HRTEM) and selected area electron diffraction (SEAD) patterns. We have performed two-terminal measurements for the Bi_2Te_3 nanostructures in different surroundings with the purpose of inspecting whether they are sensitive to the external changes. Interestingly, exposing to different chemical environment dramatically

influences the conduction and polarization properties of this material. What's more, we show that these parameters can be reversibly tuned, demonstrating that Bi_2Te_3 may find use as multifunctional sensing materials.

Results

The hexagonal Bi_2Te_3 NPs were synthesized by a solvothermal method at 180°C[22]. The XRD patterns of the as grown Bi_2Te_3 NPs are shown in Fig. S1, all of the detected peaks are indexed to the rhombohedral Bi_2Te_3 crystal system (space group: R-3m) with hexagonal cells (JCPDS card No.089-2009). Fig. 1a and b show the typical low-magnification scanning electron microscopy (SEM) images of the as-grown Bi_2Te_3 NPs. They display regular hexagonal shapes with edge lengths ranging from 300 to 450 nm. An enlarged SEM image of a representative individual Bi_2Te_3 NP is shown in the inset of Fig. 1b, where a hexagonal-shaped NP can be clearly identified. The maximum diagonal length which is twice the length of the edge is 708 nm and the interior angle is 120°. A typical transmission electron microscopy (TEM) image is shown in Fig. 1c in which the NPs exhibit flat surfaces and sharp edges. A defective NP with one ragged edge was chosen for element mapping by energy dispersive X-ray (EDX) spectroscopy on a scanning transmission electron microscope (STEM). The element maps of the overlapped areas show higher color intensities while that of the other areas are uniform. So the ripple-like patterns in the upper image are most likely resulted from bend of the NP but not overlap or thickness variation. The crystal structure of the as prepared Bi_2Te_3 NPs was investigated by high-resolution transmission electron microscopy (HRTEM) and SAED patterns. The single-crystalline nature is revealed by the continuous lattice fringes oriented in the same direction in Fig. 1e and the sharp diffraction pattern in Fig. 1g. Bulk Bi_2Te_3 has a hexagonal primitive cell with parameters a = 4.384 Å and c = 30.45 Å at room temperature[23]. The d-spacing of 0.22 nm is in good agreement with the $\{1\bar{2}10\}$ interplaner spacing of Bi_2Te_3. The diffraction pattern indicates that $<1\bar{2}10>$ is the dominate growth direction and the six side surfaces of the NP belong to the $\{1\bar{2}10\}$ family of crystallographic planes. The top and bottom surfaces are identified as the {0001} facets, which is also the mainly exposed facet. This result is consistent with the layered structure of Bi_2Te_3 in which the quintuple layer (QL) [Te1-Bi-Te2-Bi-Te1] is the fundamental building block as shown in Fig. 1f. It is considered that the bonding within one QL is covalent while that between adjacent QLs is the van der Waals forces and <0001> is the slowest growth direction[23].

We performed both two-probe and four-probe measurements on the device and the contact resistance between the probe and the Au electrode was found to be negligible (Fig. S2 in supporting informa-

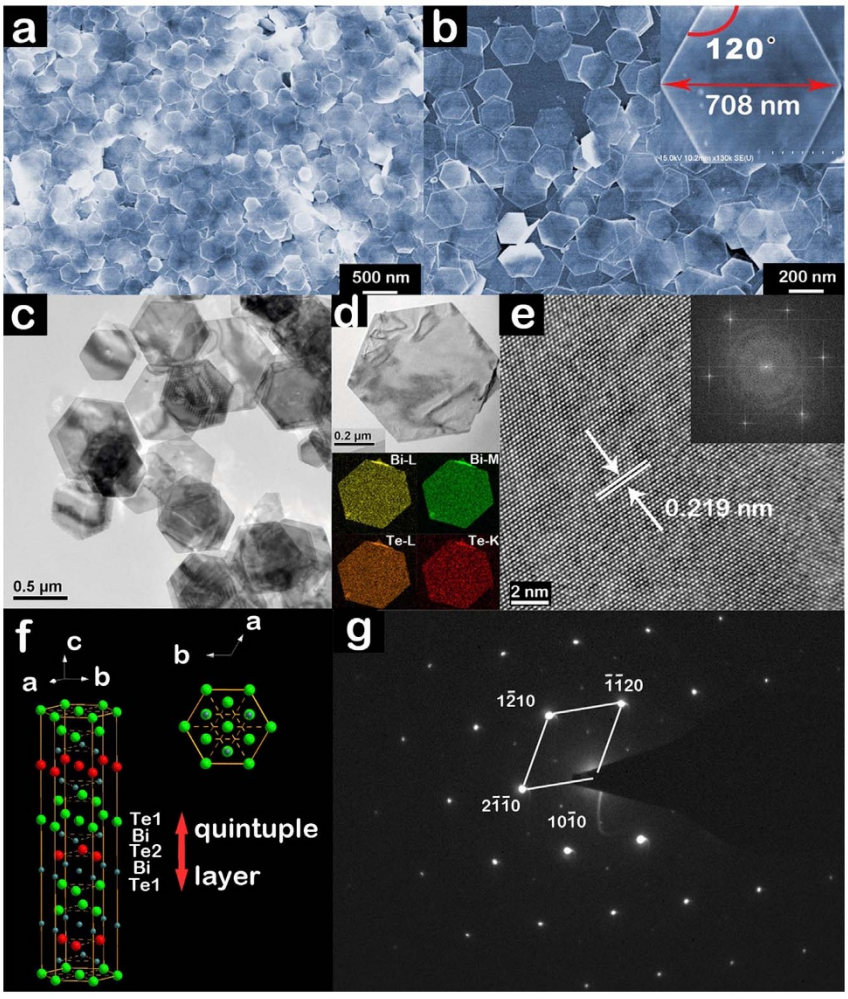

Figure 1 | Synthesis and characterizations of the hexagonal single-crystalline Bi_2Te_3 NPs exposed with {0001} facets. (a, b) Scanning electron microscopy images of the as-grown NPs. The inset in (b) is a representative individual NP. (c) TEM image of the as-grown NPs. (d) TEM image of a defective Bi_2Te_3 NP (top) and its element maps (bottom). (e) HRTEM image of the Bi_2Te_3 NP in (d) taken along the [0001] direction, revealing a high quality crystalline structure. The inset is the corresponding fast Fourier transform (FFT) image. (f) Side (left) and top (right) views of the crystal structure of Bi_2Te_3. A quintuple layer (Te1-Bi-Te2-Bi-Te1) is indicated by a double-headed arrow. (g) Selected area diffraction pattern taken along the [0001] direction.

tion). So two-probe measurements were conducted for the Bi_2Te_3 NPs under controlled environments in a metal shielded chamber (Fig. 2a and b) using a semiconductor parameter analyzer (Agilent 4156C with 1 fA current measurement resolution). A schematic of the measurment configuration is sketched in Fig. 2c and a typical photograph of the interdigital electrode is shown in Fig. 2d. The device showed nearly symmetric and linear current-voltage (I–V) characteristics, as shown in Fig. 2e. The conductance (I/V) of the device increased from 5.7 to 10.2 pS as air pressure increased from 10 to 1×10^3 Pa. Afterwards, the chamber was evacuated until the pressure was less than 1×10^{-6} torr and then refilled with high purity nitrogen (99.999%, Linde Gas Co. Ltd.). The above operation was repeated 3 times to drive away the residual air. Under the same pressure of 1×10^3 Pa, the conductance decreased from 10.2 pS in air to 0.67 pS in pure N_2. Similar results were obtained as the pressure was set to 10 or 100 Pa, that the conductance of the device in air was over 10 times larger than that in N_2 under the same pressure. This result indicates that the conducting property of the Bi_2Te_3 NPs is sensitive to the chemical content of the surrounding gas atmospheres.

A series of electrical measurements were performed on the device with an impedance analyzer (Agilent 4294A) under increasing relative humidity (RH). The relationships between the impedance (Z) and the corresponding phase angle of the device and RH are shown in Fig. 3(a,b) obtained under a 500 mV alternating voltage. In the same ambient conditions, the impedance decreased with increasing frequency, indicating that the device acted as a capactive load. The impedance changed from 100 kΩ to about 3 kΩ as the RH varied from 11% to 98% at 10 kHz, exhibiting a good sensitivity.

In order to explain the enhanced conductivity under high RH, we consider two possible mechansims that affect the transport properties of the Bi_2Te_3 NPs. At relatively low humidities, the change is ascribed to the band bending effect induced by the adsorption of water molecules, which has been experimentally discovered independently using ARPES by several other research groups[19,20]. The band bending shifts the Dirac point into the occupied states and increases the charge carrier densities at the surface, which results in the decreased impedance. But as the water molecule adsorption progresses, a continuous water layer will be formed at the surface. At this point, proton conduction will play a role in enhancing the total conductivity of the material[24,25], which can be written as:

$$H_3O^+(l,x) + H_2O(l,x') \rightleftharpoons H_2O(l,x) + H_3O^+(l,x') \qquad (1)$$

Where l denotes the liquid phase, x and x' indicate the different spatial positions. There we neglect the contribution of hydroxide (OH^-) because its mobility is much smaller than that of the protons[26]. The relationships between the capacitance and resistance of the device and RH were also measured and shown in Fig. 3(c,d). The results were obtained using the Cs-Rs measurement mode in which the sensor was treated as a two terminal device under test (DUT) composed by a resistor and a capacitor in series. In contrast to the resistance, the capacitance increases with increasing RH. This is because the capacitance reflects the dielectric property (or polarization property) of the Bi_2Te_3 NPs. Since water molecule is highly polar, the accumulation of water on the surface of the Bi_2Te_3 film increases the dielectric coefficient, which accounts for the increased capacitance. The transient responding dynamics of impedance and capacitance of the device are shown in Fig. 3(e,f). The response times (the time for the device to attain 90% of the final value) from 43% RH to 75%, 85% and 98% RHs are all less than 10 s. The transient responding characteristics at low RHs are also shown in Fig. S3. The impedance and capacitance change curves as the RH decreased step by step from 98% to 11% are shown in Fig. S4, showing the device can be used as a full range RH sensor.

To gain further information about the surrounding sensitive properties of the sensors. Ammonia was used as the probe molecule for its explicit n-doping characteristics, which had been widely used to explore the sensing properties of carbon nanotubes[27,28], graphene[29,30] and molybdenum disulfide[31,32]. The transient response of the sensor to NH_3 (0.05% to 0.4% in air) is shown in Fig. 4a. The response time τ_{res} and recovery time τ_{rec} are defined as the time required for the sensor to attain 90% of the maximum conductance change after a sudden change in the ammonia concentration. And the gas response is defined as $R = R_a/R_g$, where R_a and R_g are the resistances of the sensor in air and in the target gas, respectively.

As shown in Fig. 4b, the response exhibits an almost linear dependence on the NH_3 concentration. At relatively low NH_3 concentrations, the surface coverage is expected to be much less than a monolayer and the interaction between absorbed NH_3 molecules is negligible so it can be described by the Langmuir adsorption model. The fractional coverage θ depends on the ammonia concentration C_{NH_3} by means of the binding energy E_b[33,34]:

$$\theta = \frac{\alpha C_{NH_3}}{1 + \alpha C_{NH_3}} \qquad (2)$$

where $\alpha = \exp(E_b/k_BT)$, in which k_B is the Boltzmann's constant and T the absolute temperature. Assuming the number of NH_3 gas molecules per unit area under a monolayer coverage is ρ and the charge transfer per NH_3 molecule to Bi_2Te_3 is δ. The number of excess electrons per unit area on the surface of Bi_2Te_3 is given by $\Delta n = \rho\theta\delta$. The increased conductance can be expressed as[35]:

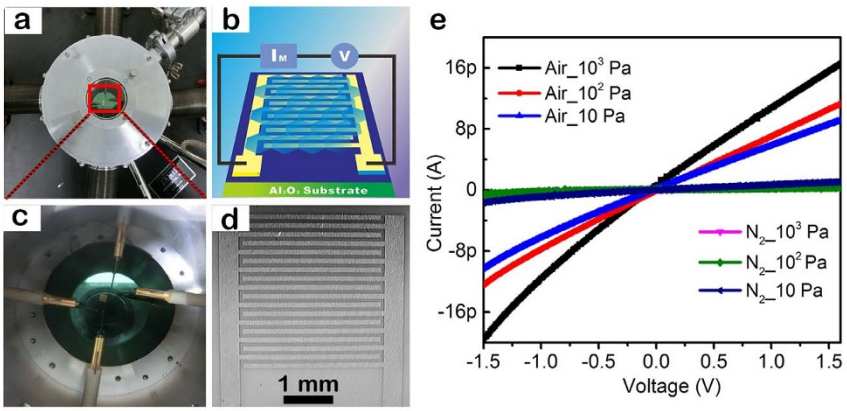

Figure 2 | Measurement configuration and electrical test results under different gas environments. (a) A photograph showing the two-probe configuration. (b) Enlarged image of the selected area in (a). (c) A simplified schematic of the testing method (applying a variable voltage on the device with the current being monitored by a high resolution source monitor unit). (d) A photograph of the interdigital electrode. (e) I–V curves of the device under different gas environments.

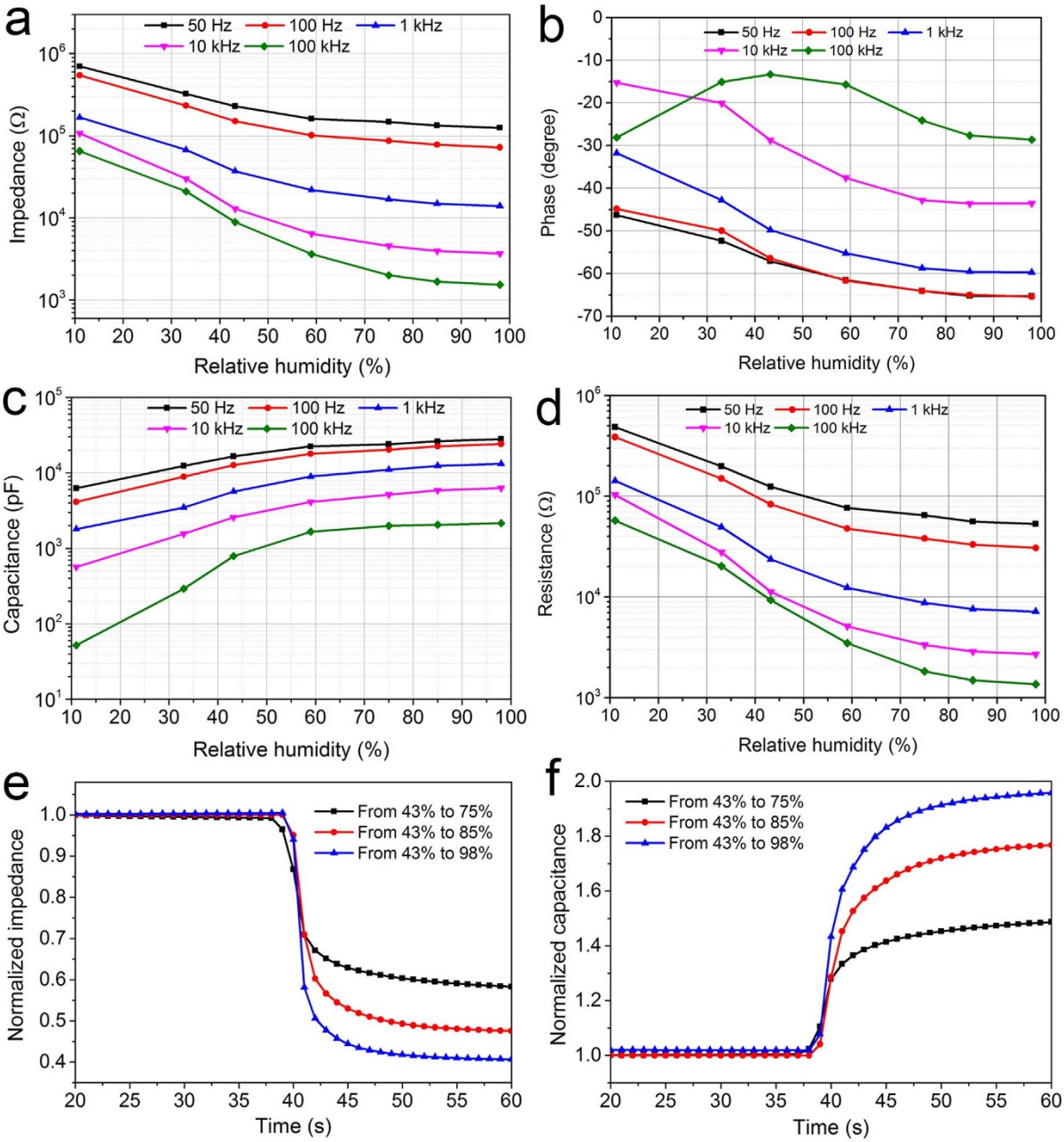

Figure 3 | Humidity sensing properties of the sensor. (a,b,c,d) The dependence of impedance, phase, capacitance and resistance of the sensor on relative humidity measured at various frequencies. (e,f) Transient response of the impedance and capacitance from 43% RH to the corresponding humidities measured at 1 kHz.

$$\Delta G^s = \mu_s e \Delta n = \mu_s e \rho \delta \frac{\alpha C_{NH_3}}{1 + \alpha C_{NH_3}} \quad (3)$$

Under low ammonia concentrations, $\alpha C_{NH_3} \ll 1$, so that ΔG^s exhibits good linear dependence on NH_3 concentration. However, this is only a very simplified model to describe the relationship between the change of conductance and gas concentration. As the concentration increases, both the repulsive interactions between the absorbed NH_3 molecules and the change in the carrier mobility can't be neglected[19,33,34,35]. The ultrafast response speed of this model sensor at room temperature is striking. The response time is 1.2 s at 0.05 vol% and becomes less than 1 s as the concentration is higher than 0.1 vol%, which is much faster than most metal oxides based NH_3 sensors, even those working at very high temperatures of 300–600°C[36]. Another interesting thing is that the response time of this sensor is much shorter than its recovery time as shown in Fig. 4c. The long recovery time indicates that NH_3 molecules are strongly bound to the Bi_2Te_3 surface and desorb very slowly. Both response time and recovery time have a tendency to decrease as the concentration of NH_3 increases, which can be explained by the higher adsorption/desorption rate resulted from the larger concentration gradients. In addition, we have fabricated another two sensors based on the Bi_2Te_3 NPs to test the repeatability of this phenomenon. As shown in Fig. 4d, the three sensors named SN-1, SN-2 and SN-3 all exhibit fast and high response to ammonia but the void IDE doesn't show any response.

Discussion

We have shown that the electric and dielectric properties of the Bi_2Te_3 NPs could be significantly changed by the outside environ-

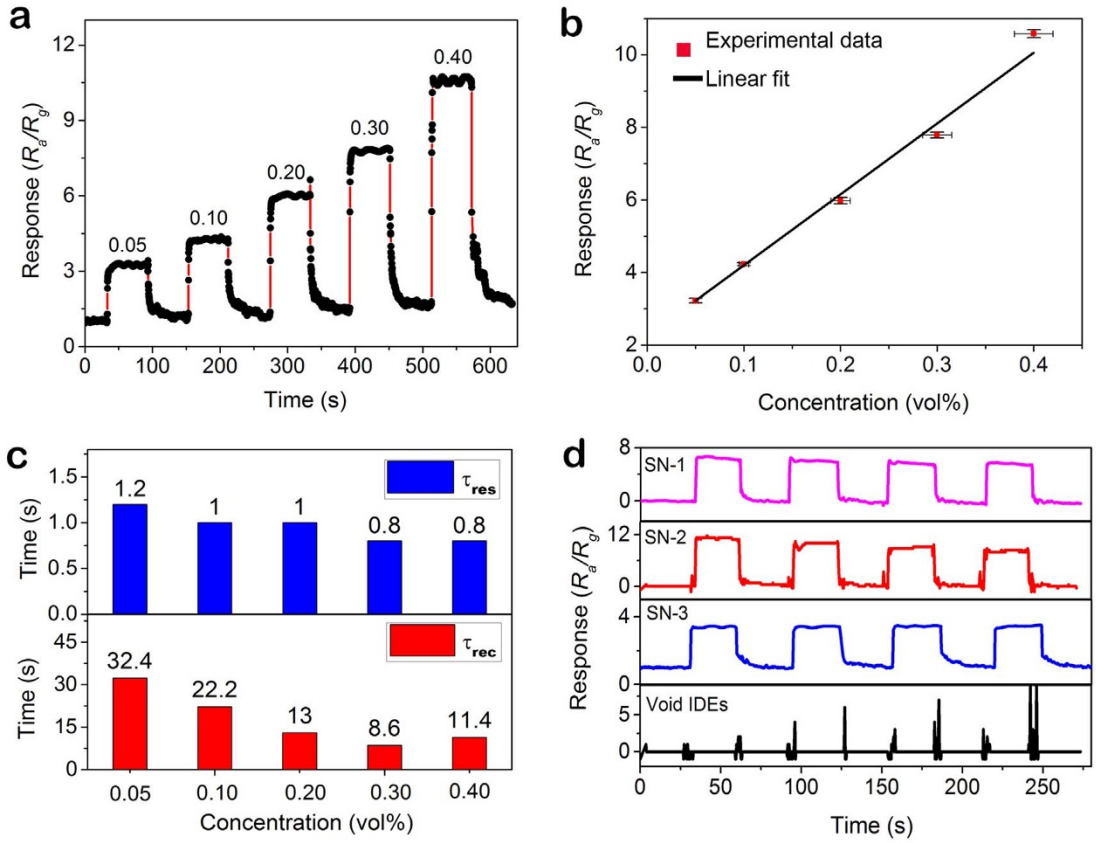

Figure 4 | Ammonia sensing characteristics of the sensor. (a) Response plots show conductance change of the Bi_2Te_3 NPs versus time with a bias voltage of 5 V at various concentrations (in vol%). (b) Sensor response as a function of NH_3 concentration. The black line indicates the fitted line. (c) Response and recovery times of the sensor at different NH_3 concentrations. (d) The response curves versus time of three model sensors made from the Bi_2Te_3 NPs to 0.4 vol% ammonia in air. The void IDE was also measured for comparison.

ments. The high, fast and reversible response indicates a high possibility and potential of this material for chemical sensing applications. Considering the function of an electronic chemical sensor is to convert a surface molecular binding event into an electric signal, TIs seem to be ideal materials for this task. This is because the conducting channels of an ideal TI exist on the surface which are directly and totally exposed to outside environment. Although the exploration of TIs for sensing is just beginning and the practical application is still quite limited, the intrinsic merits make the technological future of TIs bright. Together with the fast advances in material science and manufacturing technology, multifunctional high performance sensors based on TIs can be highly expected.

Methods

Synthesis of Single-crystalline Bi_2Te_3 NPs. The synthesis of Bi_2Te_3 NPs was achieved by a solvothermal method. Typically $BiCl_3$ (1.0 mmol, 0.315 g), Na_2TeO_3 (1.53 mmol, 0.34 g), NaOH (15 mmol, 0.6 g) and polyvinylpyrrolidone (PVP, 0.5 g) were added to ethylene glycol (EG, 36 mL) under magnetic stirring. After 1 h of stirring, the homogeneous solution was transferred to a 50 mL Teflon-lined stainless autoclave which was then sealed and heated to 180°C and maintained at this temperature for 36 h. After cooling down to room temperature, the resulting product was collected by centrifugation and washed with distilled water and ethanol each for 3 times.

Device Fabrication. Alumina ceramic was used as the substrate for its high dielectric strength and excellent chemical stability. The IDEs composed of 10 nm of titanium and 80 nm of gold with a line-width of 80 μm were fabricated by sputtering. The devices were fabricated by dropping the Bi_2Te_3 NPs dispersion onto the pre-cleaned interdigital electrodes.

Device Characterizations and Gas Sensing Measurements. The current-voltage (I–V) tests were conducted in a four-probe microscopy cryostat (JANIS ST-500) equipped with a turbo-molecular pump. The chamber pressure could be adjusted by a controlled valve. Electrical measurements were performed on a semiconductor parameter analyzer (Agilent E4156C, 1 fA/2 uV resolution). The impedance and capacitance of the device were obtained with an impedance analyzer (Agilent 4294A, 40 Hz to 110 MHz). Open and short calibration were performed with user defined kit before the measurement to ensure accuracy. The ammonia sensing test was carried out on a ZhongKe NS-4003 smart sensor analyzer under a constant voltage of 5 V.

1. Moore, J. Topological Insulators the Next Generation. *Nat Phys* **5**, 378–380 (2009).
2. Chen, Y. L. *et al.* Experimental Realization of a Three-Dimensional Topological Insulator, Bi_2Te_3. *Science* **325**, 178–181 (2009).
3. Cha, J. J. & Cui, Y. Topological Insulators the Surface Surfaces. *Nature nanotechnology* **7**, 85–86 (2012).
4. Hsieh, D. *et al.* A tunable topological insulator in the spin helical Dirac transport regime. *Nature* **460**, 1101–1105 (2009).
5. Zhao, Y. H., Hu, Y. B., Liu, L., Zhu, Y. & Guo, H. Helical States of Topological Insulator Bi2Se3. *Nano Lett* **11**, 2088–2091 (2011).
6. Arakane, T. *et al.* Tunable Dirac cone in the topological insulator Bi2-xSbxTe3-ySey. *Nat Commun* **3** (2012).
7. Zhang, H. J. *et al.* Topological insulators in Bi_2Se_3, Bi_2Te_3 and Sb_2Te_3 with a single Dirac cone on the surface. *Nat Phys* **5**, 438–442 (2009).
8. Fu, L., Kane, C. L. & Mele, E. J. Topological insulators in three dimensions. *Phys Rev Lett* **98**, 106803 (2007).
9. Hong, S. S. *et al.* Ultrathin Topological Insulator Bi2Se3 Nanoribbons Exfoliated by Atomic Force Microscopy. *Nano Lett* **10**, 3118–3122 (2010).
10. Goyal, V., Teweldebrhan, D. & Balandin, A. A. Mechanically-exfoliated stacks of thin films of Bi2Te3 topological insulators with enhanced thermoelectric performance. *Appl Phys Lett* **97** (2010).
11. Li, Y. Y. *et al.* Intrinsic Topological Insulator Bi2Te3 Thin Films on Si and Their Thickness Limit. *Adv Mater* **22**, 4002–4007 (2010).
12. Hong, S. S., Cha, J. J., Kong, D. & Cui, Y. Ultra-low carrier concentration and surface-dominant transport in antimony-doped Bi(2)Se(3) topological insulator nanoribbons. *Nat Commun* **3**, 757 (2012).
13. Kong, D. S. & Cui, Y. Opportunities in chemistry and materials science for topological insulators and their nanostructures. *Nat Chem* **3**, 845–849 (2011).
14. Chen, X., Ma, X. C., He, K., Jia, J. F. & Xue, Q. K. Molecular Beam Epitaxial Growth of Topological Insulators. *Adv Mater* **23**, 1162–1165 (2011).

15. Zhang, H. B. *et al.* Magnetoresistance switch effect of a Sn-doped Bi_2Te_3 topological insulator. *Adv Mater* **24**, 132–136 (2012).
16. Zhang, H. B., Yu, H. L. & Yang, G. W. Experimental evidence of the nanoscaled topological metallic surface state of Bi2Te3 and Sb2Te3 films. *Epl-Europhys Lett* **95**, 56002 (2011).
17. Cha, J. J., Koski, K. J. & Cui, Y. Topological insulator nanostructures. *Phys Status Solidi-R* **7**, 15–25 (2013).
18. Xiu, F. X. *et al.* Manipulating surface states in topological insulator nanoribbons. *Nature nanotechnology* **6**, 216–221 (2011).
19. Benia, H. M., Lin, C., Kernm, K. & Ast, C. R. Reactive chemical doping of the Bi_2Se_3 topological insulator. *Phys Rev Lett* **107**, 177602 (2011).
20. Zhou, B. *et al.* Controlling the carriers of topological insulators by bulk and surface doping. *Semicond Sci Tech* **27**, 124002 (2012).
21. Hasan, M. Z. & Kane, C. L. Colloquium: Topological insulators. *Rev Mod Phys* **82**, 3045–3067 (2010).
22. Zhang, Y., Hu, L. P., Zhu, T. J., Xie, J. & Zhao, X. B. High yield Bi_2Te_3 single crystal nanosheets with uniform morphology via a solvothermal synthesis. *Cryst Growth Des* **13**, 645–651 (2013).
23. Lu, W., Ding, Y., Chen, Y., Wang, Z. L. & Fang, J. Bismuth telluride hexagonal nanoplatelets and their two-step epitaxial growth. *J Am Chem Soc* **127**, 10112–10116 (2005).
24. Wan, Q. *et al.* Positive temperature coefficient resistance and humidity sensing properties of Cd-doped ZnO nanowires. *Appl Phys Lett* **84**, 3085–3087 (2004).
25. Yamamoto, S. *et al.* In situ x-ray photoelectron spectroscopy studies of water on metals and oxides at ambient conditions. *J Phys-Condens Mat* **20**, 184025 (2008).
26. Gregori, G., Shirpour, M. & Maier, J. Proton Conduction in Dense and Porous Nanocrystalline Ceria Thin Films. *Adv Funct Mater* **23**, 5861–5867 (2013).
27. Kong, J. *et al.* Nanotube molecular wires as chemical sensors. *Science* **287**, 622–625 (2000).
28. Modi, A., Koratkar, N., Lass, E., Wei, B. Q. & Ajayan, P. M. Miniaturized gas ionization sensors using carbon nanotubes. *Nature* **424**, 171–174 (2003).
29. Schedin, F. *et al.* Detection of individual gas molecules adsorbed on graphene. *Nat Mater* **6**, 652–655 (2007).
30. Fowler, J. D. *et al.* Practical Chemical Sensors from Chemically Derived Graphene. *Acs Nano* **3**, 301–306 (2009).
31. Lee, K., Gatensby, R., McEvoy, N., Hallam, T. & Duesberg, G. S. High Performance Sensors Based on Molybdenum Disulfide Thin Films. *Adv Mater* **25**, 6699–6702 (2013).
32. Late, D. J. *et al.* Sensing Behavior of Atomically Thin-Layered MoS2 Transistors. *Acs Nano* **7**, 4879–4891 (2013).
33. Romero, H. E. *et al.* Adsorption of ammonia on graphene. *Nanotechnology* **20**, 245501 (2009).
34. Gautam, M. & Jayatissa, A. H. Graphene based field effect transistor for the detection of ammonia. *J Appl Phys* **112**, 064304 (2012).
35. Checkelsky, J. G., Hor, Y. S., Cava, R. J. & Ong, N. P. Bulk Band Gap and Surface State Conduction Observed in Voltage-Tuned Crystals of the Topological Insulator Bi_2Se_3. *Phys Rev Lett* **106**, 196801 (2011).
36. Timmer, B., Olthuis, W. & Berg, A. v. d. Ammonia sensors and their applications—a review. *Sens Actuators B Chem* **107**, 666–677 (2005).

Acknowledgments

The authors would like to thank Prof. Qi-Kun Xue from Tsinghua University for helpful discussions about the device application of topological insulators. This work was financially supported by the National Basic Research Program of China (Grant No. 2007CB310500) and the National Science Foundation of China (Grant No. 61376073).

Author contributions

B.L., Q.L. and T.W. conceived the experiments. D.W. and L.W. carried out material synthesis. D.C and H.L. carried out material characterizations. Y.L. carried out the device fabrication. B.L. Y.W. and W.X. implemented electrical measurements and analysis. All authors discussed the results and contributed to writing of the manuscript.

Additional information

Supplementary information accompanies this paper at http://www.nature.com/scientificreports

Competing financial interests: The authors declare no competing financial interests.

How to cite this article: Liu, B. *et al.* Surrounding Sensitive Electronic Properties of Bi_2Te_3 Nanoplates—Potential Sensing Applications of Topological Insulators. *Sci. Rep.* **4**, 4639; DOI:10.1038/srep04639 (2014).